SHdiff/SVdiff splitting in an isotropic Earth

Dimitri Komatitsch, Lev P. Vinnik, Sébastien Chevrot

JOURNAL OF GEOPHYSICAL RESEARCH, VOL. 115, B07312, doi:10.1029/2009JB006795, 2010

SHdiff-SVdiff splitting in an isotropic Earth

Dimitri Komatitsch,[1,2] Lev P. Vinnik,[3] and Sébastien Chevrot[4]

Received 16 July 2009; revised 21 January 2010; accepted 9 March 2010; published 30 July 2010.

[1] The vertically-polarized SVdiff seismic phase sometimes arrives later than the horizontally-polarized SHdiff. Both phases propagate in the D″ layer at the base of the mantle and the difference in their arrival times is usually interpreted in terms of seismic anisotropy in D″. Using numerical simulations we demonstrate that a significant (~1 s) delay of SVdiff relative to SHdiff is present even in the IASP91 isotropic reference Earth model and in a model with a high *S* velocity in D″ relative to IASP91. The delay is accompanied by strong amplitude decay of SVdiff with distance. This relationship resembles the effect of anelasticity. In a model with a low *S* velocity in D″, the waveform of SVdiff can be very different from SHdiff, and this difference can be mistaken for a delay of SHdiff relative to SVdiff. In a laterally-heterogeneous isotropic D″ SVdiff can also be delayed because, unlike SHdiff, SVdiff has strong amplitude decay along fast paths. Its traveltime is thus dominated by slow propagation paths and tends to be positively biased. For D″ models with an *S* velocity difference of 3% between two hemispheres, there are regions where SHdiff arrives up to ~15 s earlier than the first clearly visible SVdiff. This is observed in a corridor several hundred kilometers wide. If these effects are misinterpreted in terms of D″ anisotropy in actual seismic data, estimates of anisotropy are biased and may contribute to the idea of seismic anisotropy being different in high- and low-*S*-velocity regions of D″.

Citation: Komatitsch, D., L. P. Vinnik, and S. Chevrot (2010), SHdiff-SVdiff splitting in an isotropic Earth, *J. Geophys. Res.*, *115*, B07312, doi:10.1029/2009JB006795.

1. Introduction

[2] The D″ layer atop the core-mantle boundary is a complex region of the Earth and is a focus of numerous seismic studies (for a review see, e.g., *Wysession et al.* [1998]). Large-scale (more than 1000 km) features in D″ are nearly the same in different tomographic models [e.g., *Ritsema*, 2005]. On a global scale the lowermost mantle exhibits two large low-S-velocity regions or "superplumes," one beneath the central Pacific and the other beneath the southern Atlantic and Africa. Some borders of the African superplume are sharp [*Ni et al.*, 2002]. Some large Mesozoic-Cenozoic igneous provinces and hot spots are thought to be directly related to the superplumes [e.g., *Williams et al.*, 1998; *Thorne et al.*, 2004], and there is a consensus on the correspondence between large-scale high-velocity regions in D″ and ancient subduction zones [e.g., *Dziewoński et al.*, 1977; *Hager et al.*, 1985]. The range of large-scale lateral *S* velocity variations in D″ is around ±3% [e.g., *Romanowicz*, 2008]. Beyond the large-scale features in D″ there are numerous indications of smaller-scale heterogeneities [e.g., *Luo et al.*, 2001; *Garcia et al.*, 2004; *Krueger et al.*, 1995], but the details of these features are less well constrained and often controversial [see, e.g., *Stutzmann et al.*, 2000].

[3] D″ is not only laterally heterogeneous but also anisotropic, at least in some areas [e.g., *Panning and Romanowicz*, 2004]. The usually assumed form of anisotropy in D″ is hexagonal with a vertical symmetry axis (vertical transverse isotropy or VTI). Transverse isotropy leads to a difference in travel times of the vertically and horizontally-polarized *S* waves (SV and SH, respectively). This difference is observed in the *S* waves reflected from the core-mantle boundary (the ScS seismic phase) [e.g., *Russell et al.*, 1999; *Rokosky et al.*, 2004; *Wookey et al.*, 2005] and diffracted at this boundary (Sdiff) [e.g., *Lay and Young*, 1991; *Ritsema et al.*, 1998; *Fouch et al.*, 2001; *Thomas and Kendall*, 2002; *Panning and Romanowicz*, 2004]. ScS arrives to the receiver at a time that is close to the arrival time of *S* and of some other seismic phases related to seismic boundaries in the lowermost mantle. Interpretations of the resulting interference pattern in terms of D″ anisotropy can therefore be problematic. Wave paths of Sdiff in the D″ layer can be much longer than those of ScS, which implies a larger sensitivity to the properties of D″. This is an advantage but also raises specific issues that are discussed in the present study. The nature and origin of anisotropy in D″ remained unclear until it was found that at the pressures and temperatures in D″ the silicate perovskite

[1]UMR 5212 and INRIA Magique-3D, Université de Pau et des Pays de l'Adour, CNRS, Pau, France.
[2]Institut Universitaire de France, Paris, France.
[3]Institute of Physics of the Earth, Russian Academy of Sciences, Moscow, Russia.
[4]Dynamique Terrestre et Planétaire, UMR 5562, Université Paul Sabatier, CNRS, Observatoire Midi-Pyrénées, Toulouse, France.

0148-0227/10/2009JB006795

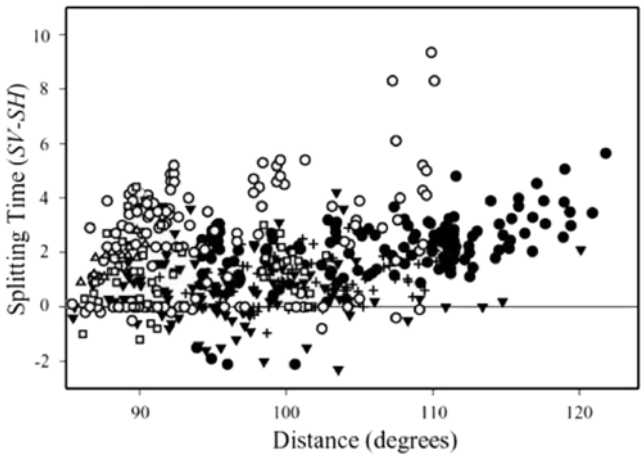

Figure 1. Copy of Figure 1c of *Moore et al.* [2004] showing SVdiff-SHdiff splitting times. The different symbols correspond to different published data sets.

is transformed into the post-perovskite phase [*Murakami et al.*, 2004; *Oganov and Ono*, 2004] with anisotropic crystals that can be preferentially oriented [e.g., *Merkel et al.*, 2007]. Thus, seismic anisotropy in D″ may provide clues to post-perovskite crystal orientations and the related mantle flow.

[4] Seismic anisotropy in D″ has been discovered in the mid-80s. *Doornbos et al.* [1986] speculated that the sheared material of D″ can be anisotropic. *Cormier* [1986] proposed that the previously-observed phase shift between the SH and SV components of ScS can be explained by anisotropy in D″, but in reality it could also be a result of azimuthal anisotropy in the upper mantle. *Vinnik et al.* [1989] observed at a distance of around 118° the Sdiff seismic phase having propagated in D″ beneath the Pacific. SVdiff was well seen and delayed relative to SHdiff by about 2 s. Previously, SVdiff, contrary to SHdiff, was seen only at distances shorter than about 105° and its properties did not attract much attention. The diagnostic properties of SKS and SKKS for azimuthal anisotropy in the upper mantle were already known [*Vinnik et al.*, 1984], and observations of SKS and SKKS in the recordings containing Sdiff indicated that the SHdiff-SVdiff discrepancy is not an effect of the upper mantle. This observation was in favor of anisotropy in D″, and later many other observations of a SHdiff-SVdiff splitting were found in support of this idea. Nowadays, measurements of SVdiff-SHdiff splitting times are available for epicentral distances from ~90° to 120° (Figure 1).

[5] *Vinnik et al.* [1989] suggested that their observations could be explained either by anisotropy in D″ or by some unspecified effects of heterogeneity. *Emery et al.* [1999] investigated the effect of small-scale (10–100 km) heterogeneities in D″ and found that they could not explain the discrepancy between SVdiff and SHdiff. Using a coupled normal-mode/spectral-element modeling technique, *To et al.* [2005] reproduced the complex waveforms of Sdiff that are observed for wave paths along the borders of the Pacific and African superplumes. They showed possible complexities of SVdiff waveforms but did not investigate SV/SH splitting. Here, using numerical models with an isotropic but heterogeneous lowermost mantle we examine the properties of SVdiff and SHdiff that can be mistaken for effects of anisotropy.

2. Modeling SHdiff and SVdiff

[6] To investigate the propagation of SVdiff and SHdiff in a laterally-heterogeneous D″ layer, we need to turn to a full-waveform numerical modeling technique. To reach periods of a few seconds, we need a method that is both precise and able to handle very large numerical meshes of the Earth. In the last decade, the spectral-element method (SEM) has proven to be well adapted to our problem: it has been successfully applied to regional seismology [see, e.g., *Liu et al.*, 2004] the full 3D Earth [see, e.g., *Komatitsch and Tromp*, 2002a, 2002b; *Chaljub and Valette*, 2004; *Chaljub et al.*, 2007] and has been used at very high resolution on large parallel machines with thousands of processors [see, e.g., *Komatitsch et al.*, 2003, 2008; *Tsuboi et al.*, 2003]. Moreover, it can accurately handle fluid-solid interfaces such as the CMB [see, e.g., *Komatitsch et al.*, 2000; *Komatitsch and Tromp*, 2002a].

[7] The largest calculations that we can currently perform for parametric studies (comparing different models) can reach a minimum period of typically 5 seconds [*Komatitsch et al.*, 2003, 2008; *Tsuboi et al.*, 2003] for a fully 3D elastic Earth. In this study we want our simulations to be accurate down to at least the same period (5 seconds). We therefore mesh the full Earth using 639,995,904 hexahedral spectral elements and we use polynomial basis functions of degree 4 to discretize the wave field inside each spectral element. This corresponds to approximately 42.2 billion grid points in the mesh and 115.1 billion degrees of freedom to compute at each iteration of the time loop of the SEM algorithm. We run the calculations in parallel on 6144 processor cores by dividing the mesh into 6144 slices having the same number of mesh elements and using message passing between computers based on the Message-Passing Interface (MPI) [see, e.g., *Gropp et al.*, 1994; *Komatitsch and Tromp*, 2002a; *Komatitsch et al.*, 2003, 2008] to exchange information between processor cores that handle mesh slices that are in contact by a common face or edge. The simulations require 0.9 gigabyte of memory per processor, i.e., a total of 5.5 terabytes. We use our SPECFEM3D software package, which is freely available from www.geodynamics.org. To simulate 33 minutes of seismograms we run the SEM for 47,200 time steps of a duration of 42 milliseconds each, which requires approximately 22 hours of elapsed time on the 6144 processor cores used in parallel.

[8] We can see that reaching such very high resolution is expensive from a numerical point of view. Viscoelasticity (anelastic attenuation) can be modeled using the SEM [see, e.g., *Komatitsch and Tromp*, 2002a], but the numerical cost in terms of both memory usage and CPU time increases by a factor of ~1.5. We therefore do not include it in our simulations. Moreover, the effects of anelastic attenuation are predictable: they are similar for SVdiff and SHdiff and do not affect the difference in travel times or spectra of SVdiff and SHdiff. In all the calculations in this article we use the IASP91 model [*Kennett and Engdahl*, 1991] with smoothed transition-zone discontinuities and the crust removed (see

auxiliary material).[1] Removing the crust in our models and smoothing the 410-km and 660-km discontinuities is a necessary step because, although these boundaries do not affect the propagation of Sdiff, they generate reverberations that, in the absence of anelastic attenuation, may contaminate the records of Sdiff. Moreover, accurate sampling of low velocities in the crust is numerically costly. Since density is not specified in IASP91 we take it from PREM [*Dziewoński and Anderson*, 1981].

[9] The source is located at the surface of the Earth at 0° latitude and longitude. It is a Centroid Moment Tensor with strike = 0°, dip = +20° and rake = +45°, which guarantees the absence of nodal lines and comparable amplitudes of SV and SH at the receivers in the equatorial zone of the eastern azimuthal sector and at the slowness of Sdiff. To obtain the displacement synthetic seismograms, the computed numerical Green functions are convolved with the Gaussian source time function $e^{-t_2/6.5}$.

3. Validation of the Method

[10] Because we are going to study in detail some small-amplitude effects for velocity models whose differences are small from a numerical point of view (±3%), we want to make sure that our numerical code is reliable to model such effects. The SEM has been validated for global seismology down to periods of 10 to 15 seconds in many articles [e.g., *Komatitsch and Tromp*, 2002a, 2002b; *Chaljub and Valette*, 2004; *Chaljub et al.*, 2007] but because of the much shorter periods involved in this study we perform a thorough verification by comparing our results for 1-D models to a normal-mode solution, to the Direct Solution Method (DSM) [*Geller and Ohminato*, 1994; *Takeuchi et al.*, 2000; *Kawai et al.*, 2006] and to a calculation of the Green's function of the Earth by Minor Integration (GEMINI) [*Friederich and Dalkolmo*, 1995], three techniques that can accurately compute the response of 1-D spherically-symmetric Earth models (only) at relatively high frequencies.

[11] It is very difficult to compute a reliable full catalog of spheroidal modes below periods of 7 or 8 seconds [e.g., *Dahlen and Tromp*, 1998, p. 301; *Kawai et al.*, 2006], although recent work seems to have improved the situation [*Al-Attar and Woodhouse*, 2008]. We therefore computed only the toroidal modes down to a period of 3.3 seconds using the Mineos2007 software package, originally written by F. Gilbert, G. Masters and J. Woodhouse [e.g., *Dahlen and Tromp*, 1998, p. 284] and modified by L. Zhao. This means that by normal-mode summation we only compute the SH component of the wave field.

[12] We compare the synthetics obtained by SEM, DSM, GEMINI and normal-mode summation along the equatorial profile at an epicentral distance of 100° for two models: our smoothed version of IASP91 [*Kennett and Engdahl*, 1991] and a modified IASP91 with the *S* velocity increased by 3% and the *P* velocity increased by 1% in D″, respectively. The thickness of D″ is 149 km. The fit of the synthetics computed by the different methods is almost perfect for both SV and SH (Figure 2). The small long-period discrepancy that can be seen between 1650 s and 1700 s probably comes from the DSM and GEMINI solutions because these methods require summation of harmonics up to very high angular orders and use a small complex damping term to accurately compute the long periods for a shallow source [*Kawai et al.*, 2006].

[13] Let us mention that in the SEM no particular assumption or simplification is made in the case of 1-D spherically-symmetric Earth models. One uses the general formulation for 3-D models [see, e.g., *Komatitsch and Tromp*, 2002a, 2002b; *Chaljub and Valette*, 2004; *Chaljub et al.*, 2007] and therefore, the SEM formulation does not "know" that the model is 1-D and we can be confident that the SEM will also be very accurate for 3-D models below.

4. SHdiff and SVdiff in 1-D Models

[14] We first explore the properties of diffracted wave fields for a few 1-D models. The thickness of the D″ layer, in which the *S* wave velocity changes with a negligible gradient from 7.27 km/s at the top to 7.30 km/s at the bottom, is 149 km. We will analyze models with ±3% and ±1% perturbations of the *S* and *P* wave speeds in D″, respectively, and a model with a doubled D″ thickness (300 km instead of 149 km) and −3% and −1% perturbations of the *S* and *P* wave speeds in D″, respectively. From now on we will show velocity instead of displacement as in Figure 2. This shifts the spectrum toward shorter periods and the resulting waveforms therefore look similar to those that are recorded by standard broad-band seismographs and used in studies of Sdiff splitting.

[15] The dominant period in the amplitude spectrum of our synthetic velocity seismograms is $\pi\sqrt{6.5} = 8$ s, and they have significant energy down to approximately 5 seconds. We will display the synthetics along the equatorial profile with a reduction slowness of 8.3 s/°, which makes Sdiff with a standard apparent velocity arrive at about the same time independently of the epicentral distance. Slower propagation is then indicated by arrival times that increase with epicentral distance, and arrival times that decrease with epicentral distance indicate a higher apparent velocity.

[16] Figures 3a, 4a and 5a show synthetics for the standard model and the model with higher velocities using true amplitudes, and Figures 3b, 4b and 5b show the same sections but with self-normalized amplitudes. Self-normalization means that each trace is normalized independently with respect to its own maximum amplitude. True amplitudes represent the amplitude decay of SVdiff and SHdiff as a function of epicentral distance in the right fashion, while self-normalization helps to see small-amplitude arrivals. In the standard model, the amplitude decay of SVdiff as a function of epicentral distance is large compared to SHdiff, and at a distance of 105° the amplitude of SHdiff becomes several times that of SVdiff (Figure 3a). Nevertheless, in the self-normalized seismograms SVdiff is well seen up to a distance of 120° (Figure 3b). The difference in amplitude decay of SVdiff and SHdiff is known from previous studies: at small epicentral distances the inefficient propagation of SVdiff is attributed mainly to a destructive interference between SVdiff and ScSV and to the large density increase at the CMB [*Chapman and Phinney*, 1972]; and in the deep shadow zone, large attenuation of SVdiff is caused by the leakage of *P* and *S* energy away from the CMB interface

[1] Auxiliary materials are available at ftp://ftp.agu.org/jb/2009jb0006795.

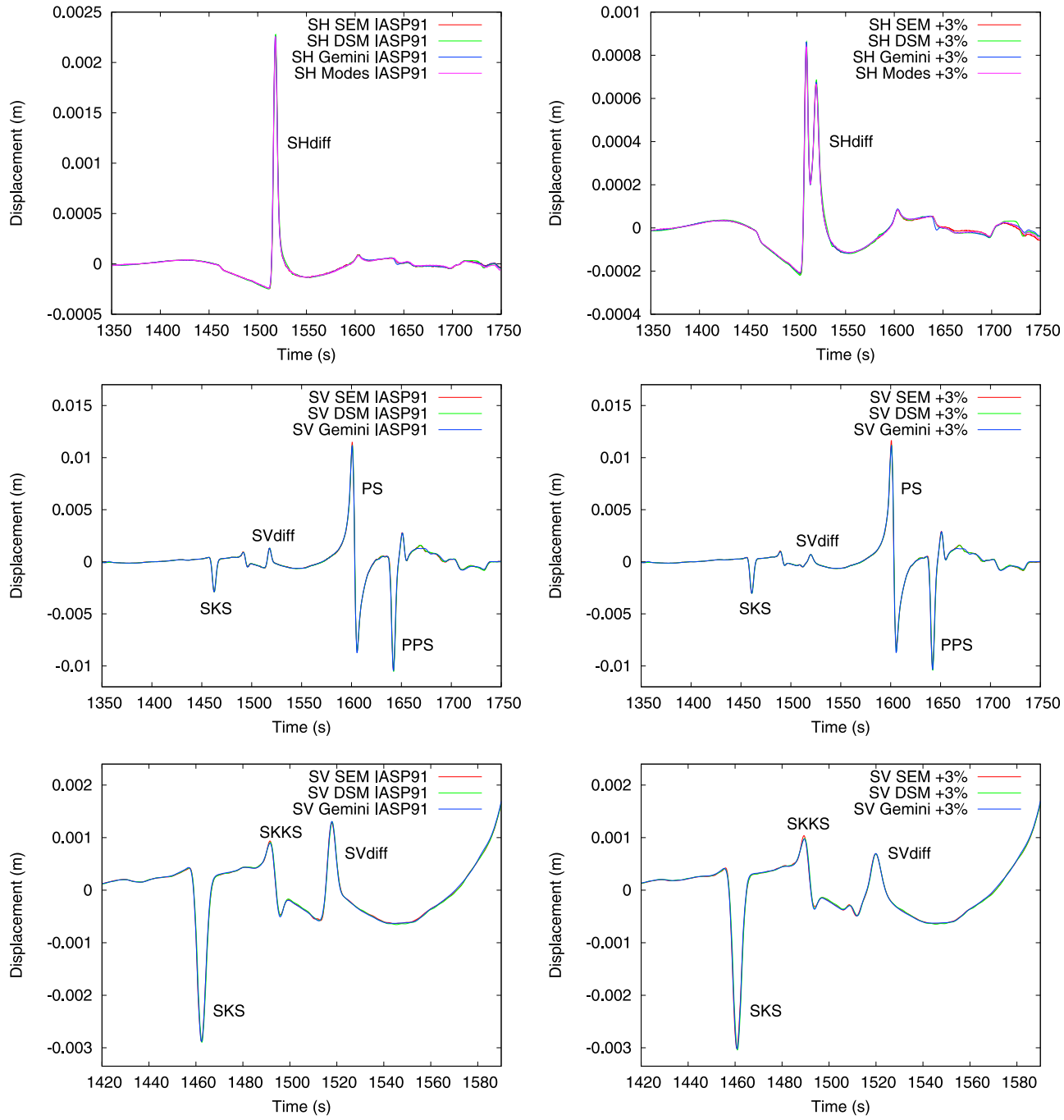

Figure 2. Comparison between SEM, DSM, GEMINI and normal-mode summation for (top) the SH displacement seismogram and (middle) the SV displacement seismogram recorded along the equatorial profile at an epicentral distance of 100° for two 1-D models: (left) our modified version of IASP91 without the crust and with smoothed mantle seismic boundaries and (right) the same model but with the *S* wave velocity increased by 3% in D″. (bottom) A close-up on SVdiff.

[*Phinney and Alexander*, 1966; *Chapman and Phinney*, 1972]. In contrast, horizontally-polarized diffracted waves are not coupled to these modes, and thus experience weaker attenuation.

[17] The self-normalized seismograms (Figure 3b) exhibit a delay of SVdiff relative to SHdiff that increases with distance from 0.0 s at a distance of 94° to 2.4 s at a distance of 120°. The related difference in slowness is ~0.1 s/°. *Doornbos and Mondt* [1979] presented theoretical estimates of Sdiff slowness for a model with a constant velocity profile in the mantle in which the difference in slowness between SVdiff and SHdiff was around 0.05 s/°. They noted that changes of this value for other realistic models are of the same order as errors in the data. Our estimate is about two times that of *Doornbos and Mondt* [1979], and, as we will see below, is model-dependent.

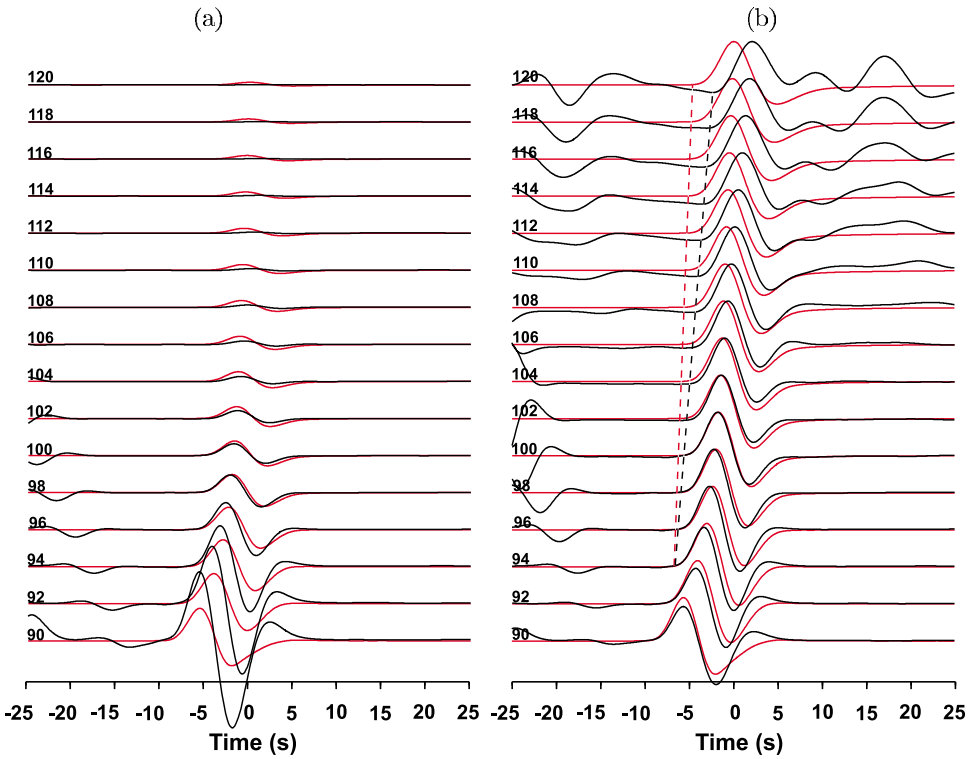

Figure 3. Synthetic velocity seismograms of SH (red) and SV (black) components along the equatorial profile for the IASP91 model: (a) with true amplitudes and (b) self-normalized amplitudes. The numbers on the left-hand side represent the epicentral distance in degrees. The red and black dashed lines indicate the arrivals of SHdiff and SVdiff, respectively. The arrival times are shown with a reduction slowness of 8.3 s/°.

[18] We note that the dominant period of SVdiff in our synthetics is somewhat shorter than that of SHdiff and, for this reason, the first SV and SH peaks are less shifted than the picked onset times. However, the difference in slowness is essentially the same for both the peaks and the onset times. Of course, the shift between the peaks of pulses with a differing dominant period can be misleading if interpreted as a travel-time difference.

[19] For comparison and further numerical validation, in Figure 4 we show the same seismograms as in Figure 3 but computed using the GEMINI code of *Friederich and Dalkolmo* [1995]. We observe the same SHdiff-SVdiff splitting, which confirms the SEM results of Figure 3.

[20] In the model with higher velocities in D″ (Figure 5a) a dominant feature in the SV component is the seismic phase that propagates with an apparent velocity of ~8.3 s/°. In our interpretation, this phase is mainly the near-critical reflection from the upper boundary of the high-velocity D″ layer, and its apparent velocity is related to the *S* velocity atop the D″ layer. SHdiff is well seen in a distance range from 92° to 120°. SVdiff is much smaller, but it is visible at distances less than ~112° in the self-normalized traces (Figure 5b). SVdiff is distinctly slower than SHdiff: at a distance of 94° they arrive almost at the same time, but at a distance of 112° the delay of SVdiff reaches 2.3 s. The difference in slowness between SVdiff and SHdiff is ~0.13 s/°, i.e., 1.3 times that of the standard model. Note that at a distance of 90° SH arrives ~3 s earlier than the first clearly visible SV. The actual arrival of SVdiff is earlier, but it is relatively weak. This effect can be described as "apparent splitting."

[21] In the model with smaller velocities in D″ (Figure 6a) SVdiff propagates with almost the same efficiency as SHdiff, and at a distance of 120° SVdiff and SHdiff are comparable in amplitude. This effect is in agreement with the theoretical results of *Phinney and Alexander* [1966] and *Doornbos and Mondt* [1979]. For this model the waveform of SVdiff at distances larger than 100° looks approximately as the derivative of SHdiff. As a result the peak in the SVdiff waveform occurs about 1.5 s earlier than in SHdiff. A broadly similar SVdiff waveform was shown by *Maupin* [1994] for a model of D″ with a negative *S* velocity gradient of -8.8×10^{-4} s^{-1}. With such a gradient the *S* velocity in D″ decreases from 7.27 km/s at the top of D″ to 7.13 km/s at the core-mantle boundary. From our computations for this model (not shown here) we found that the resulting SVdiff waveform is indeed very much the same as in Figure 6a. *Maupin* [1994] commented on this effect: "SVdiff arrives earlier than SHdiff in such a model, in disagreement with the observations of *Vinnik et al.* [1989] and *Lay and Young* [1991]." However, our synthetics in Figure 6a demonstrate that the early arrival of SVdiff is an optical effect of the waveform difference, while the actual first arrivals of SVdiff and SHdiff are synchronous and the apparent velocities are very much the same.

[22] In Figure 7 we summarize amplitude measurements for SHdiff and SVdiff for D″ with a standard thickness of

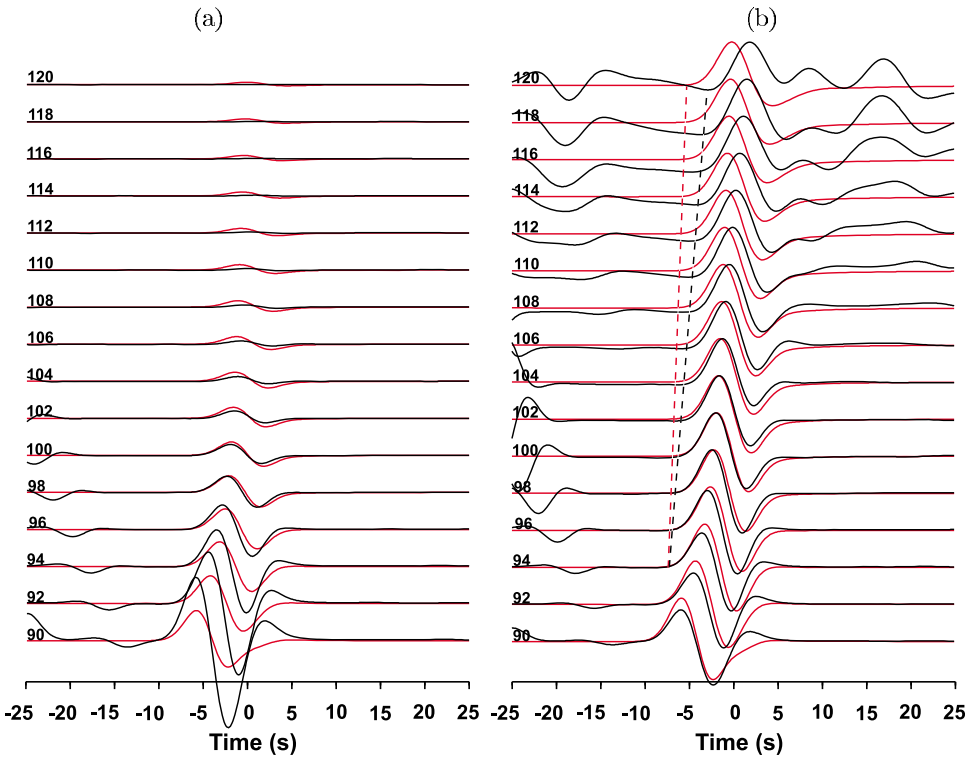

Figure 4. Same as Figure 3 but calculated with the GEMINI code of *Friederich and Dalkolmo* [1995]. The SH and SV components are red and black, respectively. The wavefield and the SHdiff-SVdiff splitting observed are very similar to those shown in Figure 3.

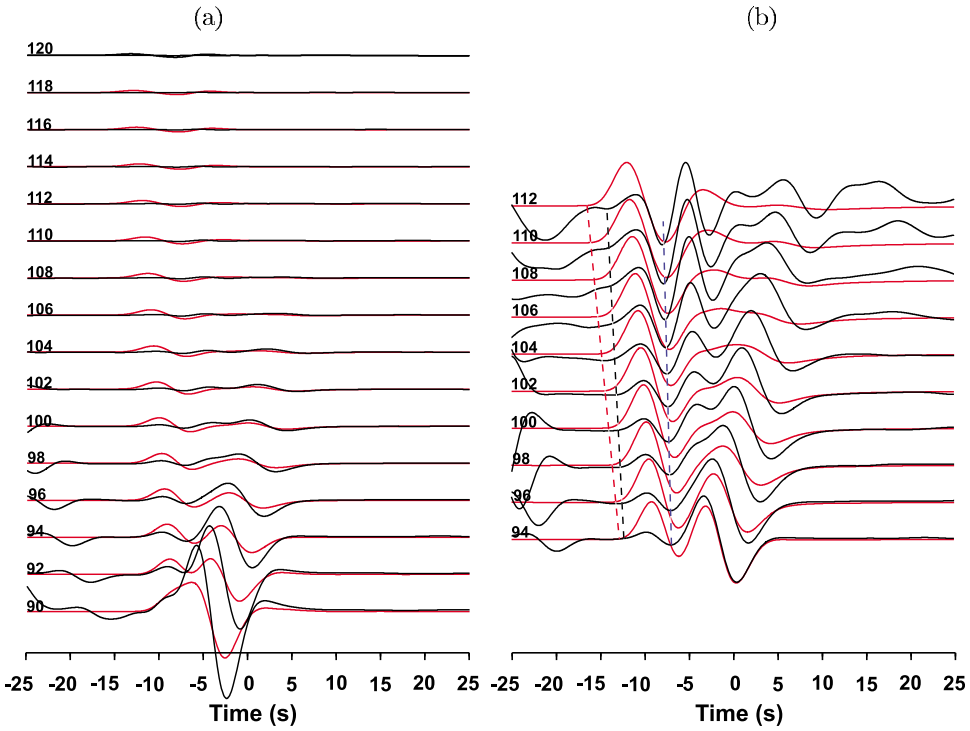

Figure 5. Same as Figure 3 but for the high-velocity D″ layer. The arrival of the near-critically reflected phase is indicated by the blue dashed line. The SH and SV components are red and black, respectively.

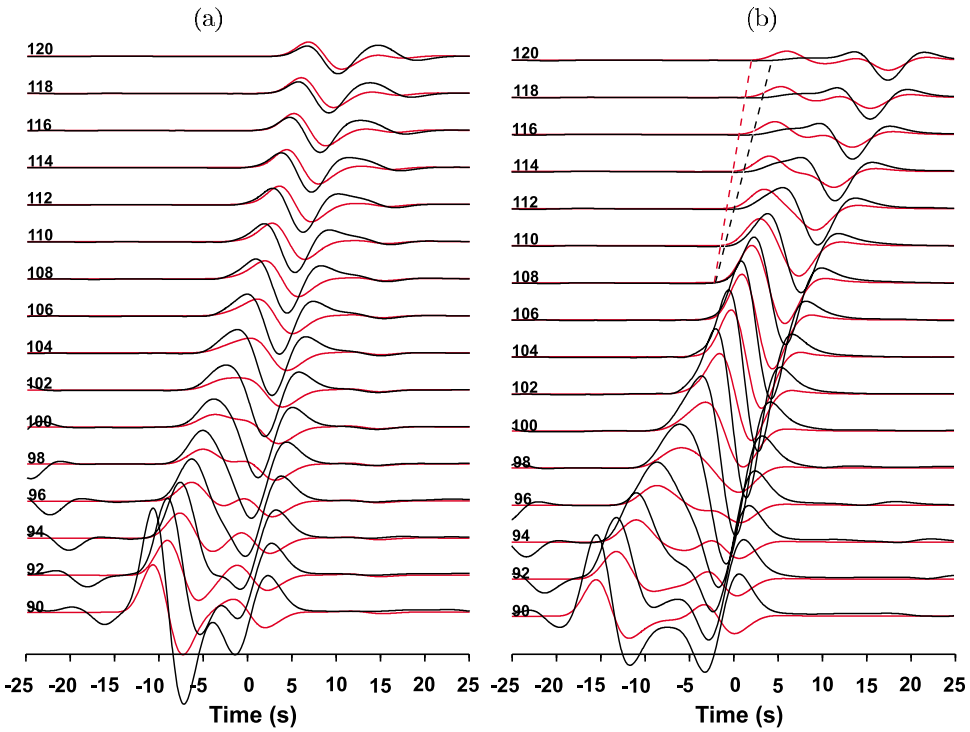

Figure 6. Synthetic velocity seismograms of SH (red) and SV (black) with true amplitudes along the equatorial profile for (a) the model with the low-velocity D″ and (b) the same model but with a double thickness of D″. The numbers on the left-hand side represent the epicentral distance in degrees. The red and black dashed lines indicate the arrivals of SHdiff and SVdiff, respectively. The arrival times are shown with a reduction slowness of 8.3 s/°.

149 km. The zero-to-peak amplitudes are normalized to unity at a distance of 90°. The amplitude decay with distance is given by the slope of the logarithmic amplitude. The large amplitude decay of both SV and SH at a distance near 90° for the high-velocity D″ is a result of constructive interference between Sdiff and the near-critical reflection from the upper boundary of D″. Outside this narrow zone the decay of SVdiff is large relative to that for the standard model, and the amplitude ratio between SV and SH is relatively small. The change in decay of SH near 95° for the low-velocity D″ is an effect of the low velocity atop the core-mantle boundary, which increases the value of the critical ray parameter and thus the critical distance beyond which shear waves are diffracted. In other words, the onset of the shadow zone is moved toward larger epicentral distances relative to the reference model. For larger velocities in D″, the effect is opposite. Amplitude decay of both SVdiff and SHdiff and their differential decay are low in the low-velocity D″ compared to the other models. Note that for D″ with a standard thickness we observe a slow propagation of SVdiff relative to SHdiff only in the models with a large amplitude decay of Sdiff (standard model and the high-velocity model). This relationship resembles the effect of anelasticity.

[23] Figure 6b shows the wave field for a model similar to the low-S-velocity model of D″ in Figure 6a but with a

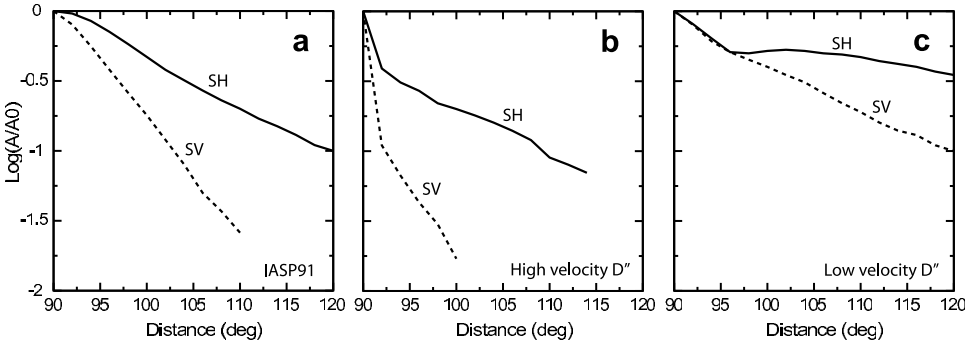

Figure 7. Normalized zero-to-peak amplitudes of SH (solid line) and SV (dashed line) measured from the synthetics in Figures 3a–6a: (a) IASP91, (b) model with the high-velocity D″, and (c) model with the low-velocity D″.

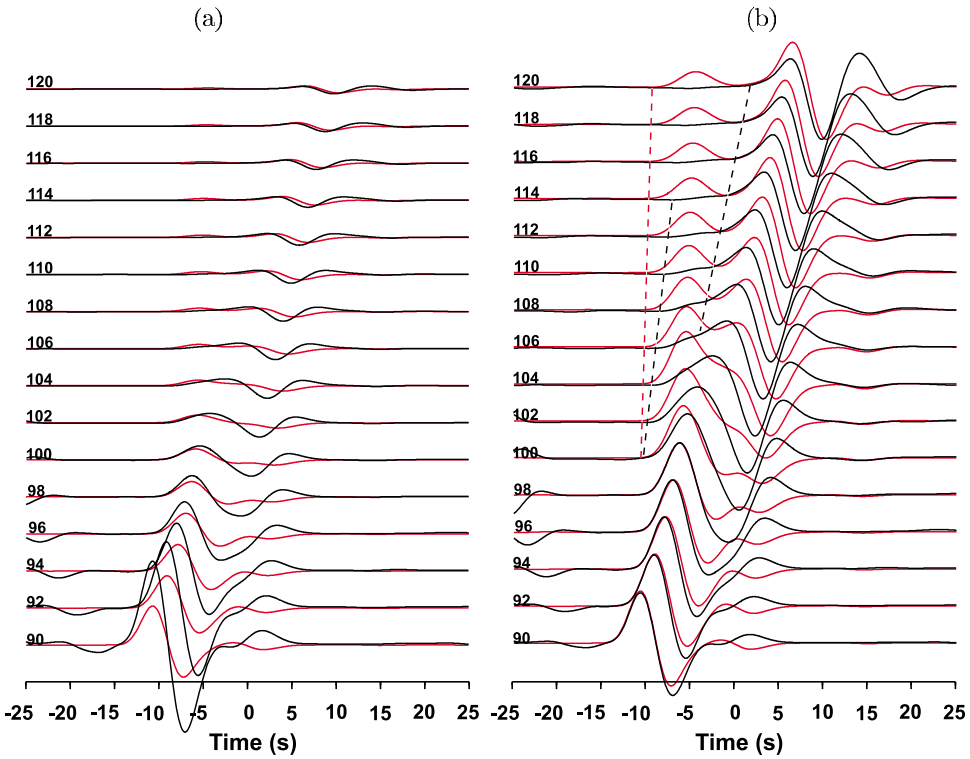

Figure 8. Synthetic seismograms of the SH (red) and SV (black) components along the equatorial profile for the laterally-heterogeneous model with the slower northern hemisphere: (a) with true amplitudes and (b) with self-normalized amplitudes. The numbers on the left-hand side represent the epicentral distance in degrees. The red and black dashed lines indicate the arrivals of SHdiff and SVdiff, respectively. The arrival times are shown with a reduction slowness of 8.3 s/°.

doubled thickness of D″ (300 km instead of 149 km). The pronounced change of the amplitude pattern at a distance of around 110° corresponds to the onset of diffraction. In the distance interval from 114° to 120° SV arrives with a delay of up to 2.0 s relative to SH; the delay is accompanied by a large amplitude decay of SV relative to SH. This relationship between the delay and attenuation for SVdiff follows the regularity found for the D″ with a standard thickness.

5. SVdiff and SHdiff in Laterally-Heterogeneous Models

[24] We now consider models with velocities that differ in the southern and northern hemispheres, each hemisphere being similar to one of the 1-D models of the previous section. We study models of D″ in which the northern hemisphere is a modified version of IASP91 (either faster or slower by 3% for the shear wave velocity) and the southern hemisphere corresponds to IASP91. Although such models are very simple compared to the true heterogeneities of D″ in the real Earth, the propagation path of Sdiff in D″ is usually only around 10° to 20° long and such models can therefore simulate Sdiff phases traveling along the edges of large natural structures such as superplumes.

[25] Along the equatorial profile in a model with a slower northern hemisphere (Figure 8) SHdiff splits into two phases of comparable amplitude, the first corresponding to the standard velocity in the southern hemisphere and the second corresponding to slower propagation in the northern hemisphere. Details of the SV wave field are better seen in the self-normalized traces (Figure 8b). SVdiff also splits into two arrivals, but the fast split wave has smaller amplitudes, longer periods, and a lower apparent velocity compared to the fast SHdiff. At a distance of 120° the first clearly visible SVdiff is delayed by 12.0 s relative to the first visible SHdiff. Synthetics along a meridional profile at a longitude of 110° (Figure 9) show that to the south of −2° SVdiff is delayed relative to SHdiff by ~1.5 s. The delay is well seen on the self-normalized traces in Figure 9b, and the wave field is similar to that for the corresponding 1-D model (IASP91) in the southern hemisphere (Figure 3). The wave field to the north of +4° is similar to that for the 1-D model in Figure 6a: SHdiff and SVdiff arrive at the same time, but the peak of SHdiff is delayed relative to SVdiff by ~1.5 s. The wave field between −2° and +4° is similar to that in the equatorial profile, which means that the corridor that is represented by the equatorial profile is about 6° wide and asymmetric. The first clearly visible SVdiff arrival can be delayed in this corridor by up to 8 s; this of course depends on the epicentral distance.

[26] For self-normalized synthetics in the equatorial profile for the model with a faster northern hemisphere (Figure 10b) at distances larger than 110°, SHdiff splits into fast and slow arrivals, with a delay of the slow phase between 6 and 9 s. SVdiff apparently splits as well, but the fast SV wave is too small relative to SHdiff to be seen clearly. The apparent velocity of the main SV phase is much smaller than expected for SVdiff. As in the 1-D model with a high-velocity

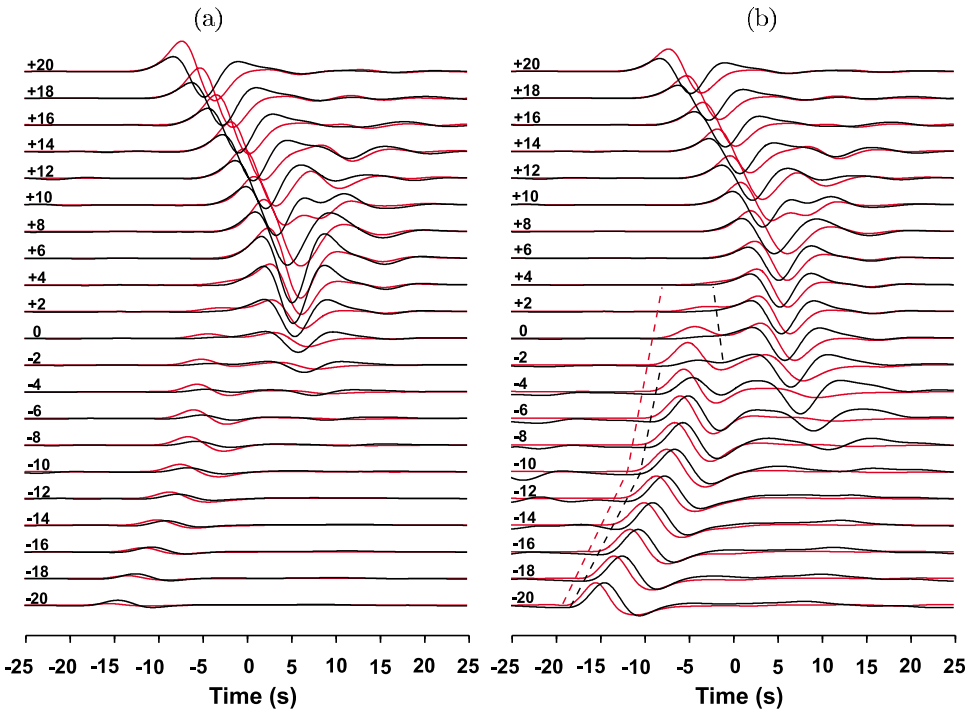

Figure 9. Same as Figure 8 but along the meridional profile located at a longitude of 110°. The northern hemisphere is slower. The SH and SV components are red and black, respectively. The numbers on the left-hand side indicate latitude in degrees. The time reduction for all traces is set to the same value, calculated for the equatorial trace.

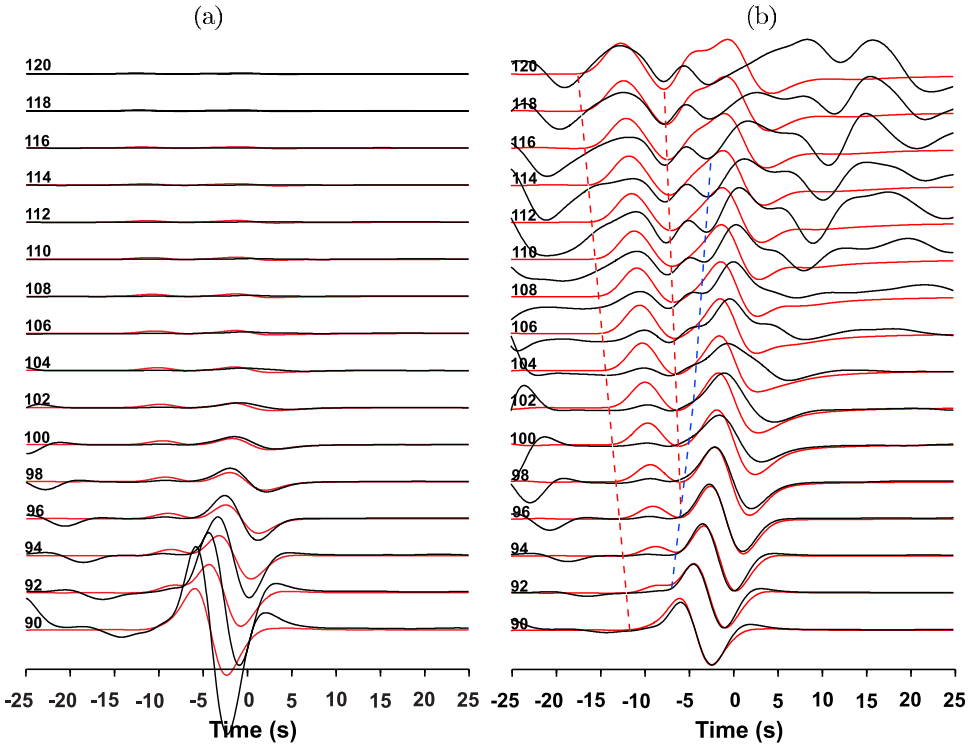

Figure 10. Same as Figure 8 but for the model with the faster northern hemisphere. The SH and SV components are red and black, respectively. The blue dashed line indicates the arrival of the near-critically reflected phase from the top of the D″ layer in the northern hemisphere.

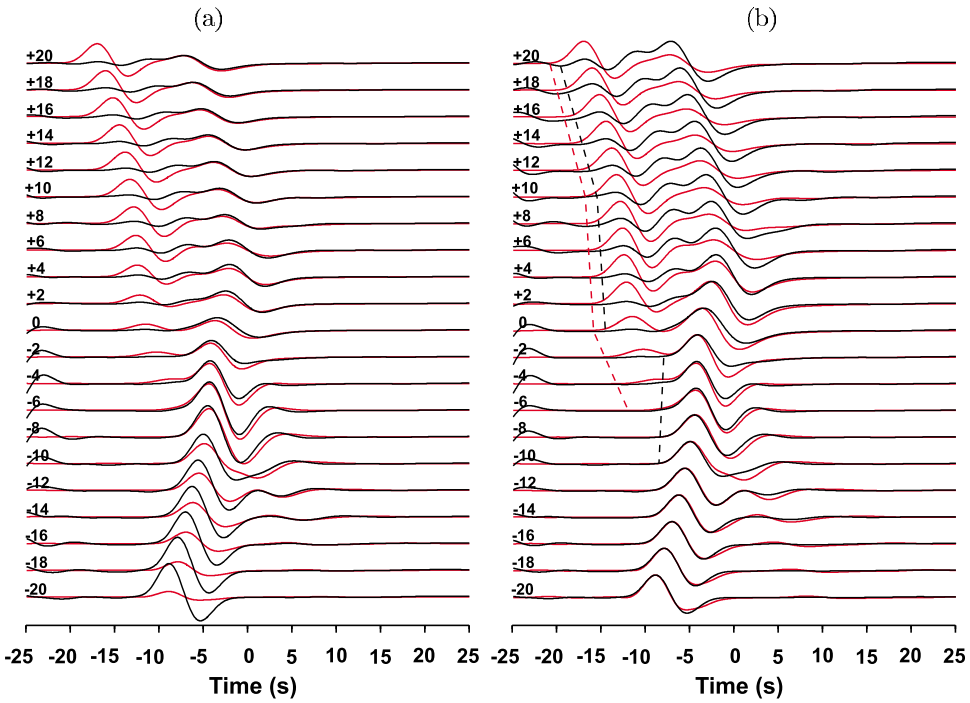

Figure 11. Same as Figure 9 but for the model with the faster northern hemisphere and along the meridional profile located at a longitude of 100°. The SH and SV components are red and black, respectively.

D″, this in our interpretation is a near-critically reflected phase from the upper boundary of the high-velocity D″ in the northern hemisphere. The delay of this SV phase relative to the fast SH is ~3 s already at a distance of 90°, and it reaches 13 s at a distance of 114°. In a meridional profile at a longitude of 100° (Figure 11) the details of the wave field are better seen in the self-normalized traces. To the south of −6° the wave field is similar to that for the 1-D standard model. The delay of SVdiff relative to SHdiff in these traces is not well seen because of the relatively small epicentral distance. To the north of 0° the wave field is similar to that for the corresponding 1-D model with a high-velocity D″ (Figure 5): SVdiff is delayed relative to SHdiff by ~1.5 s. In the interval from 0° to −6° the wave field is similar to that in the equatorial profile. As in the first laterally-heterogeneous model the corridor corresponding to the equatorial profile is 6° wide and asymmetric: it is shifted toward the hemisphere with a relatively low velocity in D″.

[27] The wave field for the low-velocity northern hemisphere with a double thickness of D″ (Figure 12) is interesting because the onset of diffraction in the northern hemisphere occurs at a large distance (around 110°, see previous Section), and a large fraction of the record section is at pre-critical distances. The thickness of D″ in the southern hemisphere was also doubled in this experiment. The record section displays the fast SHdiff in a distance range from about 96° to the end of the equatorial profile. The slow SHdiff near the end of the profile is delayed by more than 10 s. These phases correspond to the southern and the northern hemisphere, respectively. The fast SHdiff is followed by SVdiff with a lower apparent velocity: in a distance range from 100° to 116° this SVdiff is delayed by up to 2 s relative to SHdiff (at a distance of 116°). Unfortunately, this SVdiff is small in the synthetics with either true or self-normalized amplitudes. Higher amplification would be required to see it more clearly. This SVdiff is qualitatively similar to the SVdiff in the synthetics for the 1-D model IASP91 (Figure 3). The slow SHdiff is followed by SVdiff, which is delayed by up to 5 s at a distance of 120°. This delay is a combined effect of propagation in the low-velocity northern hemisphere as in Figure 6b and of inefficient propagation in the southern hemisphere as in Figure 8.

6. Discussion and Conclusions

[28] We have demonstrated that even in the 1-D isotropic IASP91 model SVdiff may arrive later than SHdiff with a delay of a few seconds (Figure 3). This effect is also observed in 1-D models with a high-velocity D″ (Figure 5) or a low-velocity D″ with a doubled thickness (Figure 6b). The delay is always accompanied by a large amplitude decay of SVdiff as a function of epicentral distance. In the low-velocity D″ with a standard thickness, amplitude decay of SVdiff is small and the delay of SVdiff relative to SHdiff is not observed (Figure 6a). The correlation between the velocity and amplitude decay of SVdiff resembles the effect of anelasticity. Note that the small amplitude of SVdiff relative to SHdiff in Figures 3 and 5 does not mean that this SVdiff cannot be seen in actual seismograms: depending on the focal mechanism, the amplitude ratio between SVdiff and SHdiff can be large in the vicinity of nodal lines for SH. Focusing/defocusing of SV and SH by lateral heterogeneities may affect this ratio as well.

[29] A different sensitivity of SVdiff and SHdiff amplitudes to the shear wave velocity in D″ leads to a specific phenomenon in a laterally heterogeneous D″: SVdiff tends

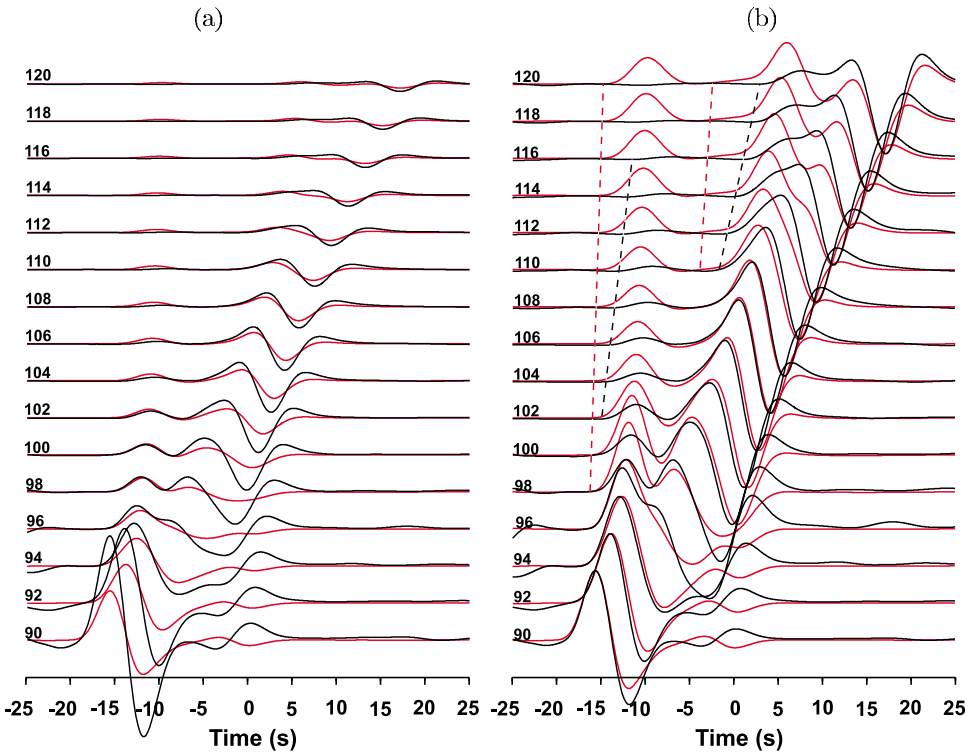

Figure 12. Same as Figure 8 but for the model with a double thickness of D″ both in the regular southern hemisphere and in the lower-velocity northern hemisphere. The SH and SV components are red and black, respectively.

to choose low-S-velocity propagation paths, whereas SHdiff propagates in both high- and low-velocity regions of D″ with comparable efficiency. As a result, SHdiff arrives earlier than the large-amplitude SVdiff phase in a broad corridor over the boundary between the high- and low-velocity regions of D″ (Figures 9 and 11). The delay of SVdiff relative to SHdiff in this corridor can reach 10 s and more.

[30] Our synthetics can now be compared with actual observations, and thus future work should focus on performing a similar study in actual tomographic models, for instance S20RTS [*Ritsema and Van Heijst*, 2000]. We will argue that in some cases isotropic D″ may present a viable alternative to interpretations of SHdiff-SVdiff splitting in terms of anisotropy in D″. At a distance of 90° the average delay of SVdiff in Figure 1 is between 1 and 2 s. A delay of ~3 s is present at this distance in Figures 5a and 10a. This is "apparent splitting" that is caused by the mistaken association of multiple arrivals. Similar delays at distances around 100° in Figure 1 are characteristic of D″ with standard or high velocities (Figures 3 and 5). Much larger delays can be inferred in a broad distance range if the SV phase, near-critically reflected from the top of the high-velocity D″, is mistaken for SVdiff (Figures 5 and 10). Large (up to 9 s) delays in Figure 1 at a distance of around 110° could be a result of this mistake. Such values are also typical for laterally-heterogeneous models (Figures 8–10). The delays of ~3 s at a distance of 120° are close to those for the low-velocity D″ with a doubled thickness (Figure 6b).

[31] A close look at some observational studies of SHdiff and SVdiff is very interesting in this respect. *Ritsema et al.* [1998] presented a large data set of observations of Sdiff sampling D″ beneath the Pacific. In a distance range from 85° to 110° the delays of SV are scattered around 0 s, but at distances between 110° and 120° the average is ~+2 s. The wave paths of the corresponding Sdiff phases are under the central Pacific, in the region of the Pacific superplume. The *S* velocity at the bottom of the mantle in this region is low and the low-velocity zone can be anomalously thick. In the synthetics for our model with the low velocity and doubled thickness of D″ (Figure 6b) the onset of diffraction is at a distance of ~110°. At larger distances SVdiff is delayed in agreement with the data of *Ritsema et al.* [1998].

[32] *Matzel et al.* [1996] found anisotropy in D″ beneath Alaska. Their source-receiver combinations span distances from 70° to 106°, but at distances smaller than 93° the SV and SH components are nearly synchronous. Beyond 93° the SV and SH shear waves often appear distinctly split. In the abstract *Matzel et al.* [1996] write: "Near 94°, SH occurs as a double arrival. SV in this range, however, remains a single arrival roughly synchronous with the second SH arrival. We have been unable to reproduce these effects in isotropic model synthetics". This description fits our seismograms in Figure 5 for the high-velocity D″. The second SH arrival, nearly synchronous with the first SV arrival, can be, in our interpretation, the near-critically reflected *S* from the upper boundary of the high-velocity D″.

[33] Most researchers find a late arrival of SVdiff relative to SHdiff, but the opposite, though rare, was reported in a few studies [e.g., *Fouch et al.*, 2001; *Pulliam and Sen*, 1998; *Panning and Romanowicz*, 2004]. In this regard the synthetics for the low-velocity D″ with a standard thickness

(Figure 6a) are of particular interest. The waveform of SVdiff for this model looks like a derivative of SHdiff: the peak of SVdiff is observed earlier than that of SHdiff, and this can be easily mistaken for the early arrival of SVdiff. There is a possibility for this mistake, but we do not want to say that it was made in the cited studies. The waveform of SVdiff in this model can lead to another mistake: a similar relation between SV and SH is characteristic of azimuthal anisotropy in the upper mantle [*Vinnik et al.*, 1984], and this may make it tempting to remove this SV by a suitable correction for upper-mantle anisotropy.

[34] Anisotropy in D″ is sometimes ascribed to ancient subducted slab material spreading along the core-mantle boundary [e.g., *Fouch et al.*, 2001]. The ancient slabs differ from the ambient mantle by higher velocities, and this hypothesis implies that anisotropy with a fast SH is a property of high-velocity regions of D″. However, the effects of propagation in isotropic D″, which can be mistaken for evidence of anisotropy, are most likely generated either in the standard (Figure 3) or high-velocity D″ (Figure 5). Large effects can also be generated in the transition zones between the regions with differing velocities (Figures 8–12). If weak VTI with a slow symmetry axis is present in both high- and low-velocity D″, in the high-velocity regions its effect can be enhanced by the isotropic effect. In the low-velocity regions the peak of SVdiff can be recorded earlier than that of SHdiff (Figure 6a). The anisotropic time shift is of opposite sign and the two effects can cancel out. As a result, a detection of anisotropy in high-velocity D″ is more likely.

[35] The analysis of post-perovskite lattice preferred orientation (LPO) by coupling numerical convection codes with calculations of plastic deformation indicates that most of the strain occurs as the subducted aggregates reach the CMB, with very little texture development above [*Merkel et al.*, 2007]. This mechanism would generate a very thin anisotropic layer atop the CMB, which is hardly reconcilable with seismic anisotropic models. The anisotropy predicted by *Merkel et al.* [2007] varies with azimuth, and SHdiff should generally be slower than SVdiff, in contrast to most seismological observations. *Duffy* [2008] suggests that the disagreement between deformation experiments and seismic observations may result from the large uncertainties in the elastic coefficients under deep mantle conditions, or from a possibility that high-temperature deformation mechanisms are different from those measured at room temperature. We hope that future improvements of seismological models will help to reconcile seismological data with deformation experiments.

[36] **Acknowledgments.** The calculations were performed on the "Jade" SGI supercomputer at CINES/GENCI in Montpellier, France, with support from Éric Boyer, Francis Daumas, Gérard Gil and also Stéphane Requena from GENCI, and on the "Titane" BULL supercomputer at CCRT/CEA/GENCI in Bruyères-le-Châtel, France, with support from Christine Ménaché, Édouard Audit, Jean-Noël Richet, Gilles Wiber, Julien Derouillat, Laurent Nguyen and Pierre Bonneau. The authors thank David Michéa and Jesús Labarta for their help to optimize the spectral-element parallel software package and Nozomu Takeuchi, Li Zhao, David Al-Attar and Nobuaki Fuji for discussions about normal-modes and the Direct Solution Method (DSM). Li Zhao kindly provided his Mineos2007 software package to compute the normal-mode solutions. The authors thank Wolfgang Friederich and the SPICE project for making the GEMINI software package available. They also thank Thorne Lay, two anonymous reviewers, associate editor Jeroen Ritsema and editor Patrick Taylor for fruitful comments that improved the manuscript. This material is based in part upon research supported by HPC-Europa project 1155 and French ANR-05-CIGC-002 NUMASIS. Lev P. Vinnik was supported by grant 07-05-00315 from the Russian Fund for Basic Research (RFBR).

References

Al-Attar, D., and J. H. Woodhouse (2008), Calculation of seismic displacement fields in self-gravitating Earth models: Applications of minors vectors and symplectic structure, *Geophys. J. Int.*, *175*(3), 1176–1208, doi:10.1111/j.1365-246X.2008.03961.x.

Chaljub, E., and B. Valette (2004), Spectral element modelling of three-dimensional wave propagation in a self-gravitating Earth with an arbitrarily stratified outer core, *Geophys. J. Int.*, *158*, 131–141.

Chaljub, E., D. Komatitsch, J. P. Vilotte, Y. Capdeville, B. Valette, and G. Festa (2007), Spectral element analysis in seismology, in *Advances in Wave Propagation in Heterogeneous Media*, *Adv. Geophys. Ser.*, vol. 48, edited by R.-S. Wu and V. Maupin, pp. 365–419, Academic, Amsterdam.

Chapman, C. H., and R. A. Phinney (1972), Diffracted seismic signals and their numerical solution, *Methods Comput. Phys.*, *12*, 165–230.

Cormier, V. F. (1986), Synthesis of body waves in transversely isotropic Earth models, *Bull. Seismol. Soc. Am.*, *76*, 231–240.

Dahlen, F. A., and J. Tromp (1998), *Theoretical Global Seismology*, Princeton Univ. Press, Princeton, N. J.

Doornbos, D. J., and J. C. Mondt (1979), Attenuation of *P* and *S* waves diffracted around the core, *Geophys. J. R. Astron. Soc.*, *57*, 353–379.

Doornbos, D. J., S. Spilopoulos, and F. D. Stacey (1986), Seismological properties of D″ and the structure of a thermal boundary layer, *Phys. Earth Planet. Inter.*, *41*, 225–239.

Duffy, T. S. (2008), Some recent advances in understanding the mineralogy of Earth's deep mantle, *Philos. Trans. R. Soc. London A*, *366*, 4273–4293, doi:10-1098/rsta.2008.0172.

Dziewoński, A. M., and D. L. Anderson (1981), Preliminary reference Earth model, *Phys. Earth Planet. Inter.*, *25*, 297–356.

Dziewoński, A. M., B. H. Hager, and R. J. O'Connell (1977), Large-scale heterogeneities in the lower mantle, *J. Geophys. Res.*, *82*, 239–255.

Emery, V., V. Maupin, and H. C. Nataf (1999), Scattering of *S* waves diffracted at the core-mantle boundary: Forward modelling, *Geophys. J. Int.*, *139*(2), 325–344.

Fouch, M. J., K. M. Fischer, and M. E. Wysession (2001), Lowermost mantle anisotropy beneath the Pacific: Imaging the source of the Hawaiian plume, *Earth Planet. Sci. Lett.*, *190*, 167–180.

Friederich, W., and J. Dalkolmo (1995), Complete synthetic seismograms for a spherically-symmetric Earth by a numerical computation of the Green's function in the frequency domain, *Geophys. J. Int.*, *122*(2), 537–550, doi:10.1111/j.1365-246X.1995.tb07012.x.

Garcia, R., S. Chevrot, and M. Weber (2004), Nonlinear waveform and delay time analysis of triplicated core phases, *J. Geophys. Res.*, *109*, B01306, doi:10.1029/2003JB002429.

Geller, R. J., and T. Ohminato (1994), Computation of synthetic seismograms and their partial derivatives for heterogeneous media with arbitrary natural boundary conditions using the Direct Solution Method, *Geophys. J. Int.*, *116*, 421–446.

Gropp, W., E. Lusk, and A. Skjellum (1994), *Using MPI: Portable Parallel Programming With the Message-Passing Interface*, MIT Press, Cambridge, Mass.

Hager, B. H., R. W. Clayton, M. A. Richards, R. P. Comer, and A. M. Dziewoński (1985), Lower mantle heterogeneity, dynamic topography and the geoid, *Nature*, *313*, 541–546.

Kawai, K., N. Takeuchi, and R. J. Geller (2006), Complete synthetic seismograms up to 2 Hz for transversely-isotropic spherically-symmetric media, *Geophys. J. Int.*, *164*(2), 411–424, doi:10.1111/j.1365-246X.2005.02829.x.

Kennett, B. L. N., and E. R. Engdahl (1991), Traveltimes for global earthquake location and phase identification, *Geophys. J. Int.*, *105*, 429–465.

Komatitsch, D., and J. Tromp (2002a), Spectral-element simulations of global seismic wave propagation—Part I. Validation, *Geophys. J. Int.*, *149*(2), 390–412, doi:10.1046/j.1365-246X.2002.01653.x.

Komatitsch, D., and J. Tromp (2002b), Spectral-element simulations of global seismic wave propagation—Part II. 3-D models, oceans, rotation, and self-gravitation, *Geophys. J. Int.*, *150*(1), 303–318, doi:10.1046/j.1365-246X.2002.01716.x.

Komatitsch, D., C. Barnes, and J. Tromp (2000), Wave propagation near a fluid-solid interface: A spectral element approach, *Geophysics*, *65*(2), 623–631, doi:10.1190/1.1444758.

Komatitsch, D., S. Tsuboi, C. Ji, and J. Tromp (2003), A 14.6 billion degrees of freedom, 5 teraflops, 2.5 terabyte earthquake simulation on the Earth Simulator, paper presented at Supercomputing SC'2003 Conference, Assoc. for Comput. Mach., Inst. of Electr. and Electr. Eng., Phoenix, 15–21 Nov.

Komatitsch, D., J. Labarta, and D. Michéa (2008), A simulation of seismic wave propagation at high resolution in the inner core of the Earth on 2166 processors of MareNostrum, *Lect. Notes Comput. Sci.*, *5336*, 364–377.

Krueger, F., M. Weber, F. Scherbaum, and J. Schlittenhardt (1995), Evidence for normal and inhomogeneous lowermost mantle and core-mantle boundary structure under the Arctic and northern Canada, *Geophys. J. Int.*, *122*(2), 637–657.

Lay, T., and C. Young (1991), Analysis of seismic SV waves in the core's penumbra, *Geophys. Res. Lett.*, *18*, 1373–1376.

Liu, Q., J. Polet, D. Komatitsch, and J. Tromp (2004), Spectral-element moment tensor inversions for earthquakes in southern California, *Bull. Seismol. Soc. Am.*, *94*(5), 1748–1761, doi:10.1785/012004038.

Luo, S.-N., S. Ni, and D. V. Helmberger (2001), Evidence for a sharp lateral variation of velocity at the core-mantle boundary from multipathed PKPab, *Earth Planet. Sci. Lett.*, *189*, 155–164.

Matzel, E., M. K. Sen, and S. P. Grand (1996), Evidence for anisotropy in the deep mantle beneath Alaska, *Geophys. Res. Lett.*, *23*(18), 2417–2420.

Maupin, V. (1994), On the possibility of anisotropy in the D″ layer as inferred from the polarization of diffracted *S* waves, *Phys. Earth Planet. Inter.*, *87*, 1–32.

Merkel, S., A. K. McNamara, A. Kubo, S. Speziale, L. Miyagi, Y. Meng, T. S. Duffy, and H. R. Wenk (2007), Deformation of (Mg,Fe)SiO3 post-perovskite and D″ anisotropy, *Science*, *316*, 1729–1732.

Moore, M. M., E. J. Garnero, T. Lay, and Q. Williams (2004), Shear wave splitting and waveform complexity for lowermost mantle structures with low-velocity lamellae and transverse isotropy, *J. Geophys. Res.*, *109*, B02319, doi:10.1029/2003JB002546.

Murakami, M. K., K. Hirose, N. Sata, Y. Ohishi, and K. Kawamura (2004), Phase transition of MgSiO3 perovskite in the deep lower mantle, *Science*, *304*, 855–858.

Ni, S. D., E. Tan, M. Gurnis, and D. V. Helmberger (2002), Sharp sides to the african superplume, *Science*, *296*, 1850–1852.

Oganov, A. R., and S. Ono (2004), Theoretical and experimental evidence for a post-perovskite phase of MgSiO3 in Earth's D″ layer, *Nature*, *430*, 445–448.

Panning, M., and B. Romanowicz (2004), Inferences on flow at the base of Earth's mantle based on seismic anisotropy, *Science*, *303*, 351–353.

Phinney, R. A., and S. S. Alexander (1966), *P* wave diffraction theory and the structure of the core-mantle boundary, *J. Geophys. Res.*, *71*, 5959–5975.

Pulliam, J., and M. K. Sen (1998), Seismic anisotropy in the core-mantle transition zone, *Geophys. J. Int.*, *135*(1), 113–128.

Ritsema, J. (2005), Global seismic structure maps, in Plates, Plumes, and Paradigms, vol. 388, edited by G. R. Foulger et al., pp. 11–18, doi:10.1130/2005.2388, Geol. Soc. Am., Boulder, Colo.

Ritsema, J., and H. J. Van Heijst (2000), Seismic imaging of structural heterogeneity in Earth's mantle: Evidence for large-scale mantle flow, *Sci. Prog.*, *83*, 243–259.

Ritsema, J., T. Lay, E. J. Garnero, and H. Benz (1998), Seismic anisotropy in the lowermost mantle beneath the Pacific, *Geophys. Res. Lett.*, *25*, 1229–1232.

Rokosky, J. M., T. Lay, E. J. Garnero, and S. A. Russel (2004), High-resolution investigation of shear wave anisotropy in D″ beneath the Cocos plate, *Geophys. Res. Lett.*, *31*, L07605, doi:10.1029/2003GL018902.

Romanowicz, B. (2008), Using seismic waves to image Earth's internal structure, *Nature*, *451*, 266–268.

Russell, S. A., T. Lay, and E. J. Garnero (1999), Small-scale lateral shear velocity and anisotropy heterogeneity near the core-mantle boundary beneath the central Pacific imaged using broadband ScS waves, *J. Geophys. Res.*, *104*(B6), 13,183–13,199.

Stutzmann, E., L. Vinnik, A. Ferreira, and S. Singh (2000), Constraint on the *S* wave velocity at the base of the mantle, *Geophys. Res. Lett.*, *27*, 1571–1574.

Takeuchi, N., R. J. Geller, and P. R. Cummins (2000), Complete synthetic seismograms for 3-D heterogeneous Earth models computed using modified DSM operators and their applicability to inversion for Earth structure, *Phys. Earth Planet. Inter.*, *119*, 25–36.

Thomas, C., and J. M. Kendall (2002), The lowermost mantle beneath northern Asia—Part II. Evidence for lower-mantle anisotropy, *Geophys. J. Int.*, *151*(1), 296–308.

Thorne, M. S., E. J. Garnero, and S. P. Grand (2004), Geographic correlation between hot spots and deep mantle lateral shear-wave velocity gradients, *Phys. Earth Planet. Inter.*, *146*, 47–63.

To, A., B. Romanowicz, Y. Capdeville, and N. Takeuchi (2005), 3D effects of sharp boundaries at the borders of the African and Pacific superplumes: Observations and modeling, *Earth Planet. Sci. Lett.*, *233*, 137–153.

Tsuboi, S., D. Komatitsch, C. Ji, and J. Tromp (2003), Spectral-element simulations of the November 3, 2002, Denali, Alaska earthquake on the Earth Simulator, *Phys. Earth Planet. Inter.*, *139*(3–4), 305–313, doi:10.1016/j.pepi.2003.09.012.

Vinnik, L. P., G. L. Kosarev, and L. I. Makeyeva (1984), Lithospheric anisotropy as indicated by SKS and SKKS waves, in *Dokl. Acad. Sci. USSR Earth Sci. Sect. Engl. Transl.*, *278*, 39–43.

Vinnik, L. P., V. Farra, and B. Romanowicz (1989), Observational evidence for diffracted SV in the shadow of the Earth's core, *Geophys. Res. Lett.*, *16*, 519–522.

Williams, Q., J. Revenaugh, and E. Garnero (1998), A correlation between ultra-low basal velocities in the mantle and hot spots, *Science*, *281*, 546–549.

Wookey, J., J. M. Kendall, and G. Ruempker (2005), Lowermost mantle anisotropy beneath the northern Pacific from differential S-ScS splitting, *Geophys. J. Int.*, *161*, 829–838.

Wysession, M. E., T. Lay, J. Revenaugh, Q. Williams, E. J. Garnero, R. Jeanloz, and L. H. Kellogg (1998), The D″ discontinuity and its implications, in *The Core-Mantle Boundary Region*, *Geodyn. Ser.*, vol. 28, edited by M. Gurnis et al., pp. 273–298, AGU, Washington, D. C.

S. Chevrot, Dynamique Terrestre et Planétaire, UMR 5562, Université Paul Sabatier, CNRS, Observatoire Midi-Pyrénées, 14 Ave. Édouard Belin, F-31400 Toulouse, France. (chevrot@dtp.obs-mip.fr)

D. Komatitsch, UMR 5212 and INRIA Magique-3D, Université de Pau et des Pays de l'Adour, CNRS, Ave. de l'Université, F-64013 Pau, France. (dimitri.komatitsch@univ-pau.fr)

L. P. Vinnik, Institute of Physics of the Earth, Russian Academy of Sciences, B. Gruzinskaya St. 10, 123995 Moscow, Russia. (vinnik@ifz.ru)